Journal of Medical Imaging

MedicalImaging.SPIEDigitalLibrary.org

Characterization and correction of intraoperative soft tissue deformation in image-guided laparoscopic liver surgery

Jon S. Heiselman
Logan W. Clements
Jarrod A. Collins
Jared A. Weis
Amber L. Simpson
Sunil K. Geevarghese
T. Peter Kingham
William R. Jarnagin
Michael I. Miga

SPIE.

Jon S. Heiselman, Logan W. Clements, Jarrod A. Collins, Jared A. Weis, Amber L. Simpson, Sunil K. Geevarghese, T. Peter Kingham, William R. Jarnagin, Michael I. Miga, "Characterization and correction of intraoperative soft tissue deformation in image-guided laparoscopic liver surgery," *J. Med. Imag.* **5**(2), 021203 (2017), doi: 10.1117/1.JMI.5.2.021203.

Journal of Medical Imaging 5(2), 021203 (Apr–Jun 2018)

Characterization and correction of intraoperative soft tissue deformation in image-guided laparoscopic liver surgery

Jon S. Heiselman,[a,b,*] Logan W. Clements,[a,b] Jarrod A. Collins,[a,b] Jared A. Weis,[c] Amber L. Simpson,[d] Sunil K. Geevarghese,[e] T. Peter Kingham,[d] William R. Jarnagin,[d] and Michael I. Miga[a,b]
[a]Vanderbilt University, Department of Biomedical Engineering, Nashville, Tennessee, United States
[b]Vanderbilt University, Vanderbilt Institute for Surgery and Engineering, Nashville, Tennessee, United States
[c]Wake Forest School of Medicine, Department of Biomedical Engineering, Winston-Salem, North Carolina, United States
[d]Memorial Sloan-Kettering Cancer Center, Hepatopancreatobiliary Service, Department of Surgery, New York, New York, United States
[e]Vanderbilt University Medical Center, Division of Hepatobiliary Surgery and Liver Transplantation, Nashville, Tennessee, United States

Abstract. Laparoscopic liver surgery is challenging to perform due to a compromised ability of the surgeon to localize subsurface anatomy in the constrained environment. While image guidance has the potential to address this barrier, intraoperative factors, such as insufflation and variable degrees of organ mobilization from supporting ligaments, may generate substantial deformation. The severity of laparoscopic deformation in humans has not been characterized, and current laparoscopic correction methods do not account for the mechanics of how intraoperative deformation is applied to the liver. We first measure the degree of laparoscopic deformation at two insufflation pressures over the course of laparoscopic-to-open conversion in 25 patients. With this clinical data alongside a mock laparoscopic phantom setup, we report a biomechanical correction approach that leverages anatomically load-bearing support surfaces from ligament attachments to iteratively reconstruct and account for intraoperative deformations. Laparoscopic deformations were significantly larger than deformations associated with open surgery, and our correction approach yielded subsurface target error of 6.7 ± 1.3 mm and surface error of 0.8 ± 0.4 mm using only sparse surface data with realistic surgical extent. Laparoscopic surface data extents were examined and found to impact registration accuracy. Finally, we demonstrate viability of the correction method with clinical data. [DOI: 10.1117/1.JMI.5.2.021203]

Keywords: laparoscopy; soft tissue deformation; biomechanical modeling; image-guided surgery; registration; liver.

Paper 17264SSR received Sep. 7, 2017; accepted for publication Nov. 21, 2017; published online Dec. 14, 2017.

1 Introduction

In comparison with the traditional open approach, laparoscopic liver resections are associated with significant patient benefits, such as reduced blood loss, shorter duration of hospital stay, and fewer postoperative complications with no detriment to overall mortality or oncological adequacy.[1,2] However, the learning curve for laparoscopic liver resection is considerable, and it is estimated that 10% of all major laparoscopic liver resections require intraoperative conversion to an open approach.[3] Uncontrollable bleeding and unintentional damage to surrounding structures are the causes of conversion in 38% of all converted cases; an additional 5% of converted cases are attributed to concern over oncological margins.[4] Liver resection requires determination of which vessels to spare or interrupt in the context of patient-specific vasculature and tumor positions.[5,6] However, the ability to localize subsurface vessels and tumors using traditional palpation techniques is impaired during laparoscopy, and these errors may be an important factor contributing to the high rate of laparoscopic-to-open conversion. Currently, the laparoscopic approach for hepatic resection critically depends on the skill and experience of the surgeon due to the high complexity and steep learning curve of the procedure. Recent consensus recommendations have suggested that intraoperative guidance using preoperative images could be a useful tool for visualizing subsurface anatomy, determining the resection plane, and navigating laparoscopic resection.[7] With its potential to assist with these challenging tasks, image guidance could facilitate more complex laparoscopic procedures, reduce the risk of complications, and potentially extend patient candidacy for laparoscopic resection.

To date, conventional image-guided approaches have been limited for laparoscopic liver surgery. Approaches that have been investigated typically utilize rigid registrations, which cannot account for intraoperative soft tissue deformation.[8–13] One major source of deformation in laparoscopic procedures is the process of insufflation where the abdominal cavity is pressurized with carbon dioxide. Insufflation has been shown to cause distension and displacement of the ventral wall and diaphragm,[14,15] to which the liver is attached by the falciform ligament and the left and right triangular ligaments, respectively [Fig. 1(a)]. During insufflation, these ligaments are pulled into tension as the abdominal cavity expands. Intraoperative deformation is further complicated by the choice of dissecting any number of these ligaments depending on the degree of organ mobilization required. While deformations exceeding

*Address correspondence to: Jon S. Heiselman, E-mail: jon.s.heiselman@vanderbilt.edu

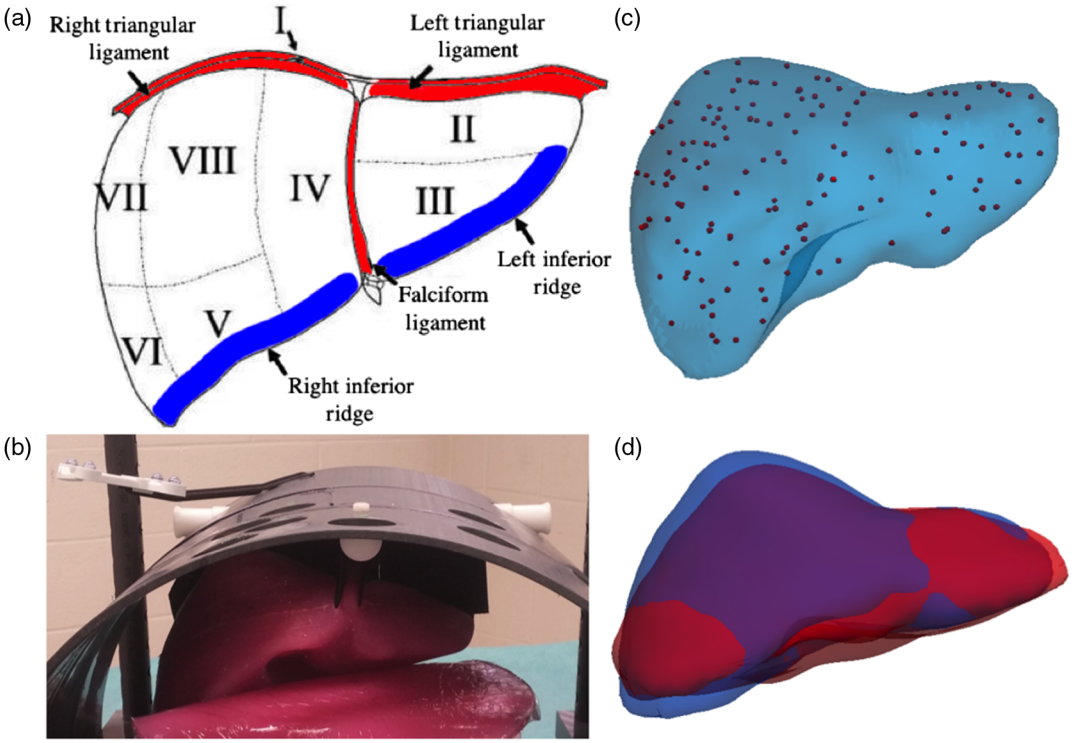

Fig. 1 (a) Anatomy of the liver, adapted from Kingham et al. The falciform and left and right triangular ligament attachments shown in red are put in tension during insufflation due to expansion of the abdominal cavity. Two salient anatomical features of the liver are shown in blue. (b) The liver phantom is suspended in an insufflated mock abdomen without mobilization from its ligaments. (c) Positions of the 147 subsurface targets distributed throughout the volume of the phantom. (d) Segmented preoperative and intraoperative phantom volumes are shown in blue and red, respectively. The difference between surfaces demonstrates the deformation reproduced in the laparoscopic phantom simulator.

11 mm have been observed in porcine livers in response to insufflation,[16,17] no clinical analysis of liver deformation during laparoscopy has been performed. The first aim of this work is to quantify the amount of deformation attributed to the laparoscopic approach from a series of 25 clinical laparoscopic-to-open conversions.

Several approaches for correcting deformation have been developed for image-to-physical registration using partial liver surfaces. Masutani and Kimura[18] proposed an early method that used free-form deformation modes to match the preoperative shape of the liver to a patch of intraoperative surface data. Cash et al.[19] developed a linear elastic biomechanical model constrained by closest point boundary conditions to register the preoperative liver to intraoperative surface data. Dumpuri et al.[20] improved this method by applying a surface Laplacian equation to extrapolate closest point distances from sparse intraoperative data onto the model. In recent years, nonrigid registration methods have been developed for the laparoscopic environment. Allan et al.[21] developed a nonrigid registration method to stereo-reconstructed laparoscopic surfaces using coherent point drift.[22] Suwelack et al.[23] employed a model that mixed elastic mechanical response with electrostatic attractive forces to match the shapes of preoperative and intraoperative models of the liver. A more recent publication by Plantefève et al.[24] established a laparoscopic nonrigid registration pipeline that produced a dynamic elastic registration from tracked texture landmarks. Another variant reported by Reichard et al.[25] projected spring force boundary conditions from a stereo-reconstructed depth map onto a biomechanical model. However, these approaches either fail to use mechanics-based models[18,21,22] or treat deformation correction through direct application of digitized intraoperative surfaces as boundary conditions.[19,20,23–25] While the former methods do not accurately model deformation beyond the immediate neighborhood of intraoperative data, the latter methods may not adequately align regions with poor data localization and can have unfavorable responses to untreated sources of intraoperative surface noise. Additionally, stereo vision surface reconstructions and feature tracking can become unpredictable in the presence of specular highlights and laparoscope illumination, blood covering intraoperative surfaces, occlusion by laparoscopic tools, and surgical smoke from electrocautery.[26] A more robust approach is to reconstruct a solution from a constrained set of possible deformations that are expected to occur on the basis of anatomical support of the organ, as opposed to using surface data to directly apply boundary conditions to the model. Rucker et al.[27] addressed this by proposing an inverse method that optimized an initially unknown polynomial family of displacement boundary conditions applied to an anatomical support surface that serves as the mechanical foundation for intraoperative liver deformation. This method has been shown to be effective at correcting intraoperative deformation in open clinical practice.[28]

In this work, we adopt the anatomically constrained comprehensive surface reconstruction strategy explored by Rucker et al. but report a realization of biomechanical boundary conditions for the purpose of laparoscopic nonrigid registration, with two key contributions. First, as opposed to open surgery where only one support surface exists, the laparoscopic configuration of

the liver is mechanically supported by four distinct regions: the falciform, the left and right triangular ligament attachments, and the organ posterior where the liver makes contact with the bowel. We reformulate boundary conditions using a control point strategy that allows any number of independent support surfaces to be considered. Our correction method is based on establishing a set of deformations that are expected to result from intraoperative loads applied to the laparoscopic support surfaces where forces are conducted to the organ. Second, our reformulation makes no underlying assumption about the functional form of displacement boundary conditions and consequently the resulting displacement solution over the support surfaces. This reconceptualization of support surface interactions is intended to improve the fidelity of the model-reconstructed deformation. The second aim of this work is to evaluate our proposed correction framework in a series of phantom and clinical experiments.

2 Methods

Our dual aims of measuring and correcting laparoscopic deformation consist of four parts: (1) characterization of the intraoperative liver surface during clinical cases of laparoscopic-to-open conversion, (2) reproduction of realistic laparoscopic deformations in a controllable phantom, (3) evaluation of intraoperative deformation in clinical and phantom data, and (4) deformation correction using intraoperative sparse surface data in retrospective clinical and phantom datasets.

2.1 *Clinical Data Collection*

The clinical data used throughout this work originate from a previous study by Kingham et al.[9] A total of 32 patients were enrolled in a protocol approved by the institutional review board at Memorial Sloan-Kettering Cancer Center wherein a laparoscopic staging procedure was performed prior to an open resection under image guidance. From segmented preoperative CT or MRI images, three-dimensional (3-D) model surfaces of the liver were generated using surgical planning software (Scout™ Liver, Analogic Corporation, Peabody, Massachusetts). Tetrahedral meshes were created from these liver surfaces using customized software for mesh generation.[29] With the intention of eventual conversion to open laparotomy, intraoperative laparoscopic exploration was performed to gauge the severity and resectability of disease. During this exploratory step, the falciform ligament was dissected to expose the anterior surface of the liver. Sparse representations of the anterior surface and anatomical features of the liver were then collected with an optically tracked laparoscopic stylus through a minimally invasive surgical guidance system (Explorer™ MIL, Analogic Corporation, Peabody, Massachusetts).[10] Liver surface and feature data were collected at a standard insufflation pressure of 14 mm Hg then at a reduced insufflation pressure of 7 mm Hg. Following conversion to open, these digitizations were repeated. All collections were performed during apneic phases induced at end-expiration to minimize the impact of respiratory motion.[30] These digitizations provide an anatomically labeled sparse 3-D point cloud of the shape of the intraoperative organ surface. Whereas the study by Kingham et al. aimed to directly compare the accuracy of image-to-physical rigid registrations between laparoscopic and open surgical approaches, in this work, the laparoscopic and open surface collections are used to quantify the magnitudes of liver deformation among preoperative, laparoscopic, and open organ configurations (Sec. 2.3), as well as to demonstrate clinical feasibility of our correction approach (Sec. 3.2). To enable paired statistical comparisons across intraoperative conditions, this study uses 25 of the previously reported 32 patients that possessed intraoperative data under all three intraoperative scenarios of both laparoscopic insufflation pressures and open approach.

2.2 *Phantom Data Collection*

Intraoperative surgical constraints make obtaining a sufficient amount of clinical data for subsurface validation of registration algorithms particularly challenging. Therefore, a tissue-mimicking phantom and abdominal frame were created to reproduce laparoscopic deformations.[31] In brief, a mock abdomen was constructed at insufflated dimensions, and nine laparoscopic access ports were placed in clinically relevant positions. Mock detachable falciform and triangular ligaments were used to suspend a liver phantom inside the abdomen, with partial support provided by a simulated bowel structure on the organ posterior. Figures 1(a) and 1(b) show the anatomical attachments to the liver and the deformation experienced by the phantom in the laparoscopic simulator. Through suspending the phantom in the enlarged abdominal cavity and removing ligament attachments, intraoperative deformations associated with a fixed insufflation level and adjustable organ mobilization can be reproduced. With the phantom, three states of intraoperative deformation were considered: no mobilization, left mobilization, and right mobilization. The falciform and the left or right triangular ligaments were removed for left or right mobilization, respectively. No ligament attachments were removed for the no-mobilization condition.

The phantom was constructed from 50% Ecoflex® 00-10 platinum-cure silicone mixed with 30% Silicone Thinner® and 20% Slacker® Tactile Mutator (Smooth-On Inc., Pennsylvania). A total of 147 radiopaque target beads were placed throughout the volume by carefully pouring the silicone around a network of threads to which the beads were weakly adhered by a thin layer of petroleum jelly. The threads were withdrawn from the cured silicone, leaving the target beads distributed as shown in Fig. 1(c). The segmented positions of these beads in pre- and postdeformation CT images allow validation of target error after registration. The phantom was molded after a physical liver 3-D printed from a preoperative patient CT. A predeformation, preoperative image of the phantom was taken before demolding. In the same manner as the clinical cases, the predeformation CT was segmented and a preoperative organ model was generated. Intraoperative deformation was applied by suspending the phantom from its ligament attachments in the abdominal frame. Left and right mobilizations were performed as previously described to produce three configurations of intraoperative deformation in total. A postdeformation CT image was acquired for each scenario, and sparse digitizations of the anterior surface and salient features were collected through the nine access ports in the abdominal enclosure using a tracked laparoscopic stylus and tracked conoscope (ConoPoint-10, Optimet Inc., Jerusalem, Israel).[32,33] Segmented pre- and postdeformation CT liver phantom volumes are shown in Fig. 1(d).

2.3 *Evaluation of Intraoperative Deformation*

Our clinical intraoperative data for each patient at three phases of laparoscopic-to-open conversion enable tracking of organ surface deformation for each individual liver throughout the

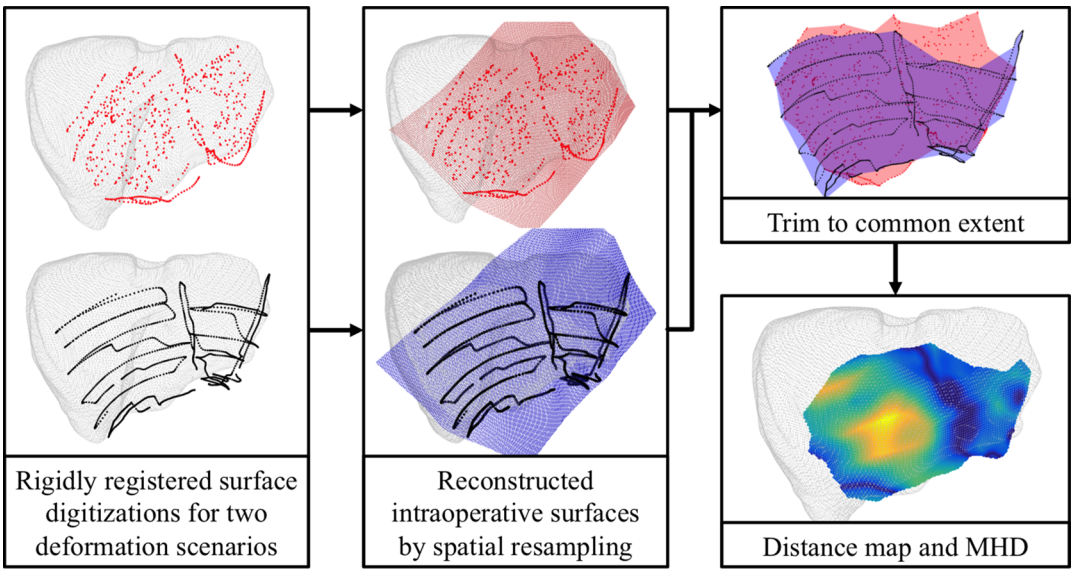

Fig. 2 Overview of intraoperative organ shape comparison. Sparse point clouds of the intraoperative organ shape under two distinct operative conditions are coregistered to the preoperative liver surface and resampled into full reconstructed surfaces. Distance measures of shape dissimilarity are computed for only the resampled points that are enclosed by the extents of both data sources (purple region).

operation. The sparse surface data collected during the laparoscopic and open approaches are representative of organ shape at each of the three intraoperative conditions: laparoscopic high insufflation pressure (Lap14mmHg), laparoscopic low insufflation pressure (Lap7mmHg), and open approach (Open). Our objective is to quantify the magnitude of deformation existing among pairs of organ conformations, done by coregistering and reconstructing full surfaces from sparse data as summarized in Fig. 2.

2.3.1 *Rigid registration*

To compare the deformation between two sparse surfaces, registration to a common reference frame is needed. For each patient, all intraoperative point clouds were rigidly registered to the surface of the preoperative liver using a salient feature-weighted iterative closest point algorithm.[34] This registration method takes advantage of preoperatively and intraoperatively designated anatomical labels to bias closest point correspondence such that salient anatomical features preferentially align. This registration method is preferred since it produces consistent coregistrations even in the presence of significant deformation. The salient features used in this study include the falciform ligament and the left and right inferior ridges. The algorithm produces a rigid transformation that minimizes the feature-weighted distance between the preoperative surface and the intraoperative data points. We should also note that following rigid registration to the preoperative liver, we employ a spatial resampling strategy to reconstruct more complete surfaces of the deformed intraoperative organ shapes from sparse sets of points. This approach was reported in previous work with a detailed analysis of how it improves fidelity of both rigid and nonrigid registration.[35]

2.3.2 *Shape comparison metric*

The modified Hausdorff distance (MHD) metric[36] is chosen to characterize the difference between organ surfaces as a quantification of surface deformation. MHD is an appropriate metric for its ability to measure average shape distortion. Briefly reviewed here, for two sets of points X and Y, MHD is defined as the maximum of the average closest point distance from every point in X to any point in Y and the dual average closest point distance from Y to X

$$\overline{d}_{\mathrm{CP}}(X,Y) = \frac{1}{|X|}\sum_{\mathbf{x}\in X} \min_{\mathbf{y}\in Y}(\|\mathbf{x}-\mathbf{y}\|), \tag{1}$$

$$\mathrm{MHD} = \max[\overline{d}_{\mathrm{CP}}(X,Y), \overline{d}_{\mathrm{CP}}(Y,X)]. \tag{2}$$

While the MHD metric can underpredict in situations with large discrepancies between surface curvatures,[37] these circumstances would require either misregistration or unrealistic deformation and are not expected to occur.

2.4 *Deformation Correction Strategy*

The overarching strategy to correct for soft tissue deformations is shown in Fig. 3 with the goal of producing an accurate volumetric alignment between the preoperative organ data and the intraoperative organ presentation. Anatomical support surfaces that bear intraoperative load are identified on the preoperative image-derived biomechanical model and control point selections are designated on these surfaces. A set of predicted deformations are precomputed from displacement perturbations of each control point, creating an effective Jacobian that measures the change in deformation across the mesh with respect to control point motion. Intraoperatively, the shape of the preoperative liver is fit to sparse intraoperative surface data by iteratively solving for a linear combination of model-predicted deformations using the Levenberg–Marquardt nonlinear optimization method. Finally, a model relaxation is performed to locally improve the registration near the support surfaces. These steps are described in more detail in the following sections.

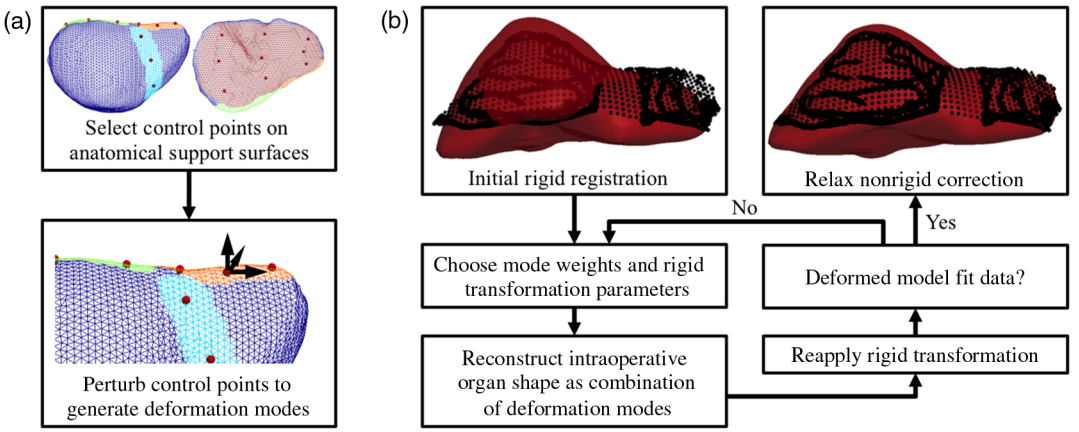

Fig. 3 Overview of deformation correction algorithm. (a) Model solutions are computed for perturbations of a choice of control points. (b) Nonrigid correction is performed by iteratively updating a set of parameters that are used to reconstruct the intraoperative organ shape from precomputed modes of expected deformation.

2.4.1 *Finite element model*

A finite element model was employed to simulate deformation on a preoperatively constructed tetrahedral mesh. The model is governed by the standard Navier–Cauchy constitutive equations for linear elasticity in three dimensions

$$\frac{E}{2(1+\nu)(1-2\nu)}\nabla(\nabla\cdot\mathbf{u})+\frac{E}{2(1+\nu)}\nabla^2\mathbf{u}+\mathbf{F}=0, \tag{3}$$

where $\mathbf{u}$ is the displacement for each node in the mesh, $\mathbf{F}$ is the applied force distribution, E is Young's modulus, and ν is Poisson's ratio. This system of partial differential equations is solved via the Galerkin weighted residual method using linear Lagrange basis functions and the assumption of isotropic material properties consistent with Rucker et al. This approach enables the model displacements to be solved from the linear system of equations

$$K\mathbf{u}=\mathbf{F}, \tag{4}$$

where K is the global stiffness matrix. However, in a major departure from the approach used by Rucker et al., where a family of *a priori* polynomial displacement solutions were prescribed to a single support surface, in our proposed approach we instead apply independent control point perturbations as displacement boundary conditions on four separate anatomical support surfaces.

2.4.2 *Control point selection*

The falciform ligament, the left and right triangular ligaments, and the posterior surface are modeled as support surfaces where intraoperative forces influence the liver. Boundary faces associated with these four supports are designated on the mesh of the preoperative liver. Control points are chosen on the support surfaces by parameterizing a curve $\mathbf{p}(s)$ to each ligament support and a surface $\mathbf{q}(s,t)$ to the posterior support such that

$$\mathbf{p}(s)=\begin{cases}x(s)=\sum_{i=0}^{P}a_i s^i\\ y(s)=\sum_{i=0}^{P}b_i s^i\\ z(s)=\sum_{i=0}^{P}c_i s^i\end{cases}, \tag{5}$$

$$\mathbf{q}(s,t)=\begin{cases}x(s,t)=\sum_{i=0}^{P}\sum_{j=0}^{i}a_{ij}s^{i-j}t^j\\ y(s,t)=\sum_{i=0}^{P}\sum_{j=0}^{i}b_{ij}s^{i-j}t^j\\ z(s,t)=\sum_{i=0}^{P}\sum_{j=0}^{i}c_{ij}s^{i-j}t^j\end{cases}, \tag{6}$$

where $P=5$ is the order of fit and $a\in\mathbf{A}_s$, $b\in\mathbf{B}_s$, and $c\in\mathbf{C}_s$ are the linear weights for the polynomial subspace of each support surface parameterization. For each point $\mathbf{x}_j$ in the support surface x_s, the parameter s_j is determined by normalizing the distance from $\mathbf{x}_j$ to the point $\mathbf{x}^*\in x_s$ that is most distant from the centroid of the support

$$s_j=\frac{\|\mathbf{x}_j-\mathbf{x}^*\|}{\max(\|\mathbf{x}_j-\mathbf{x}^*\|)}. \tag{7}$$

The parameter t_j is established by normalizing the distance from $\mathbf{x}_j$ to $\mathbf{p}(s_j)$ by a curve parameterized to either the upper boundary nodes of the support surface $\mathbf{p}^+(s)$ or the lower boundary nodes $\mathbf{p}^-(s)$, depending on the position of $\mathbf{x}_j$ relative to $\mathbf{p}(s)$ such that $t_j\in[-1,1]$

$$t_j=\frac{\|\mathbf{x}_j-\mathbf{p}(s_j)\|}{\|\mathbf{p}^{\pm}(s_j)-\mathbf{p}(s_j)\|}. \tag{8}$$

The vectors of weights $\mathbf{A}_s$, $\mathbf{B}_s$, and $\mathbf{C}_s$ are solved using ordinary least squares such that the support surface parameterizations best fit the positions of the n_s vertices on the mesh that belong to each support surface

$$X(s)=\begin{bmatrix}1 & s_1 & s_1^2 & \cdots & s_1^P\\ 1 & s_2 & s_2^2 & \cdots & s_2^P\\ \vdots & \vdots & \vdots & \ddots & \vdots\\ 1 & s_{n_s} & s_{n_s}^2 & \cdots & s_{n_s}^P\end{bmatrix}, \tag{9}$$

$$X(s,t) = \begin{bmatrix} 1 & s_1 & t_1 & \cdots & s_1 t_1^{P-1} & t_1^P \\ 1 & s_2 & t_2 & \cdots & s_2 t_2^{P-1} & t_2^P \\ \vdots & \vdots & \vdots & \ddots & \vdots & \vdots \\ 1 & s_{n_s} & t_{n_s} & \cdots & s_{n_s} t_{n_s}^{P-1} & t_{n_s}^P \end{bmatrix}, \tag{10}$$

$$[\,\mathbf{A}_s \quad \mathbf{B}_s \quad \mathbf{C}_s\,] = (X^T X)^{-1} X^T x_s. \tag{11}$$

An M number of control points are evenly spaced across each dimension of the parameterized supports by finding the closest vertices on the mesh to $\mathbf{p}(s)$ or $\mathbf{q}(s,t)$ at interior grid points created by dividing s and t into $M+1$ intervals. A parameter sweep across the placement of 1 to 5 control points on each ligament attachment site and 3 to 48 control points on the posterior support surface showed that no significant difference existed over target registration error (TRE) in the phantom among these choices of control points ($p > 0.9$, one-way analysis of variance; maximum change of 0.5 mm). A choice of $M = 3$ control points on the laparoscopic support surfaces of the liver, as shown in Fig. 3(a), was selected.

2.4.3 *Generation of deformation modes from displacement boundary conditions*

Forward model solutions to 1 mm displacement perturbations in the x-, y-, or z-directions of each control point are simulated keeping all other control points stationary and all other nodes stress free. These solutions produce a set of intraoperative deformation modes that estimate linear gradients to point load perturbations of the support surface. The resulting displacement, stress, and strain solutions establish the rows of the $3n \times k$ Jacobian matrix J_u and the $6n \times k$ Jacobian matrices J_σ, and J_ε, respectively, where n is the number of nodes in the mesh and k is triple the number of control points, equal to the total number of perturbations made. These Jacobian matrices can be precomputed and used to quickly estimate intraoperative deformations. A parameter vector $\boldsymbol{\alpha}$ of length k is determined such that a linear combination of the deformation modes estimates the intraoperative node displacements, stresses, and strains

$$\mathbf{u} = J_u \boldsymbol{\alpha}, \tag{12}$$

$$\boldsymbol{\sigma} = J_\sigma \boldsymbol{\alpha}, \tag{13}$$

$$\boldsymbol{\varepsilon} = J_\varepsilon \boldsymbol{\alpha}. \tag{14}$$

The average strain energy density $\bar{U}$ associated with a particular deformation configuration is calculated as

$$\bar{U} = \frac{1}{2}\boldsymbol{\sigma} \cdot \boldsymbol{\varepsilon} = \frac{1}{2}\boldsymbol{\alpha}^T (J_\sigma^T J_\varepsilon)\boldsymbol{\alpha}. \tag{15}$$

This approach can be employed because the use of a linear model gives rise to the principle of superposition. Namely, because the model is a linear system, the response to any possible change over the anatomical support surfaces is identical to the sum of responses to less complex inputs that span the total change. While we recognize that our point load perturbations do not span all possible distributed loads that may be applied to the support surfaces in truth, this assumption is needed to reduce the complexity of the inverse problem to make optimization of $\boldsymbol{\alpha}$ tractable under intraoperative time constraints. Furthermore, our approximation of the intraoperative distributed load as a statically equivalent combination of point loads is justified by Saint Venant's principle, which states that the difference between the responses to two statically equivalent loads vanishes exponentially with the distance from the load.[38] Hence, the model reconstruction is accurate in the far field, although it may experience local artifacts in the near-field on the support surfaces. A treatment to resolve this situation is described in Sec. 2.4.5.

2.4.4 *Reconstruction of intraoperative deformation*

Our nonrigid registration is performed through an intraoperative optimization to find the set of model perturbations that best fit the resampled surface data. An alignment of the preoperative model to sparse intraoperative data is initialized with a salient feature-weighted rigid registration method as described in Sec. 2.3.1. After rigid registration, the salient feature and anterior surface digitizations are resampled using the surface reconstruction method described by Collins et al.[35] This resampling method standardizes the density and topology of the sparse surfaces to diminish the influences of trajectory, dwell, and surface noise from intraoperative data collection. An augmented vector of model parameters $\boldsymbol{\alpha}'$ is considered, where

$$\boldsymbol{\alpha}' = [\boldsymbol{\alpha}^T, t_x, t_y, t_z, \theta_x, \theta_y, \theta_z]^T \tag{16}$$

includes the rigid body translation and rotation parameters t_x, t_y, t_z, θ_x, θ_y, and θ_z in addition to the vector of linear coefficients $\boldsymbol{\alpha}$ that apply to the preoperatively determined responses to control point deformations. The corrected node positions $\mathbf{x}_c$ are taken to be

$$\mathbf{x}_c = T(\mathbf{x}_0 + J_u \boldsymbol{\alpha}), \tag{17}$$

where $\mathbf{x}_0$ are the node positions of the original preoperative mesh and T is the rigid body transformation defined by the optimized translation and rotation parameters.

In a similar manner to the approach proposed by Rucker et al., we employ an implementation of the Levenberg–Marquardt method[39] to find an $\boldsymbol{\alpha}'$ that minimizes a nonlinear objective function Ω based on model-data surface error regularized by strain energy

$$\Omega = \frac{1}{N}\sum_{i=1}^{N} w_i \|\mathbf{x}_{d,i} - \mathbf{x}_{c,i}\|^2 + \kappa \bar{U}^2, \tag{18}$$

where N is the number of resampled data points, w_i is an additional weighting factor for salient feature points, $\mathbf{x}_{d,i}$ is an indexed point in the resampled intraoperative surface data, and $\mathbf{x}_{c,i}$ is the closest point on the model surface to $\mathbf{x}_{d,i}$ rapidly queried using a k-d tree. We use a strain energy regularization constant of $\kappa = 10^{-8}$ in agreement with the characterization done by Rucker et al. The Levenberg–Marquardt update step to the parameter vector is performed iteratively, where

$$\boldsymbol{\alpha}'_{k+1} = \boldsymbol{\alpha}'_k + [J^T J + \lambda\, \mathrm{diag}(J^T J)]^{-1} J^T \mathbf{r}, \tag{19}$$

until an absolute tolerance of $|\Omega_{k+1} - \Omega_k| < 10^{-12}$ is reached. The vector of residuals for our objective function is

$$\mathbf{r} = [\sqrt{w_1/N}\|\mathbf{x}_{d,1} - \mathbf{x}_{c,1}\|, \ldots, \sqrt{w_N/N}\|\mathbf{x}_{d,N} - \mathbf{x}_{c,N}\|, \sqrt{\kappa}\bar{U}]^T. \quad (20)$$

The augmented Jacobian of residuals $J = \partial\mathbf{r}/\partial\boldsymbol{\alpha}'$ is computed using a forward finite difference approximation, and the damping parameter $\lambda > 0$ is updated using a trust region prediction ratio framework. We should note that Eq. (16) represents a simultaneous iterative optimization of both rigid and nonrigid components of the registration. With this approach, some effects associated with rigid body rotation that can compromise linear models are diminished. Conventionally, these effects are usually compensated by a corotational finite element formulation,[40] which accounts for local rotational effects at the element level. In the algorithm above, instead, the bulk rotation is determined per iteration. The advantage to this approach is that precomputation of a set of model solutions is still enabled.

2.4.5 *Model relaxation*

As previously discussed, due to the use of control point perturbations, model-reconstructed deformations may encounter local inaccuracies around the immediate vicinities of the applied perturbations. These artifacts may appear within the support surface regions that are represented by the control points in place of more complete distributed loads, although their influence rapidly vanishes with distance. To diminish their effect in the near-field, we have developed a model relaxation step that consists of a forward model solution to Eq. (4) with boundary conditions consisting of a partial solution to the optimized model correction computed in Sec. 2.4.4. The solved displacements at surface nodes that do not belong to a support surface are applied directly as Dirichlet boundary conditions while the remaining surface nodes near the control points are left unconstrained. This step serves to relax the solutions over the support surfaces to the most stable model-predicted distributed loads that produce the far-field response best matching the intraoperative data. As a result, the displacement solutions over the support surfaces are not required to be of any specific functional form, such as the truncated bivariate polynomial used by Rucker et al.

3 Experimental Evaluation

3.1 *Evaluation of Intraoperative Deformation*

For each patient, MHD was computed between pairs of organ surface data taken from presentations at 14-mm Hg insufflation (Lap14mmHg), 7-mm Hg insufflation (Lap7mmHg), open (Open) surgical configurations, and the rigidly registered anterior liver surface as segmented from the preoperative CT scan (Preop). Table 1 shows the organ surface MHD between preoperative, laparoscopic, and open surgical phases. A series of one-sample t-tests determined that all distributions of MHD were found to significantly differ from zero (all $p < 10^{-5}$; Bonferroni's multiple comparison $\alpha = 0.008$), indicating that substantial shape change occurred between each pair of interrogated operative surfaces. This shows that significant deformation occurs between (a) preoperative and intraoperative phases, (b) laparoscopic and open surgical approaches, and (c) standard and reduced levels of insufflation pressure. This last statement is especially important because it strongly suggests that insufflation has a significant impact on laparoscopic deformation of the liver.

Table 1 MHD (mean ± std) in mm between preoperative, laparoscopic, and open operative conditions. The shape changes associated with each sequential step in the laparoscopic-to-open conversion appear along the first diagonal. The cumulative shape change relative to the preoperative organ is shown in the top row.

	Preop	Lap14mmHg	Lap7mmHg	Open
Preop	0	10.1 ± 5.9	9.0 ± 7.0	7.4 ± 4.6
Lap14mmHg	—	0	6.4 ± 2.6	6.6 ± 3.3
Lap7mmHg	—	—	0	6.3 ± 2.5
Open	—	—	—	0

In examining the relative magnitudes of deformation between each operative transition using paired t-tests, we find that the MHD in the initial transition from the preoperative to laparoscopic organ configuration is significantly larger than subsequent intraoperative changes where insufflation pressure is lowered ($p = 0.0012$) or where the surgical approach is converted to open ($p = 0.0011$). Meanwhile, the differences in MHD associated with lowering insufflation pressure and converting to open are similar ($p = 0.76$). This suggests that the largest proportion of intraoperative deformation is associated with the initial preoperative-to-intraoperative transition, coinciding with the timing of when preoperative surgical plans would be needed to determine resection planes.

We also find that in comparison with the preoperative liver shape, the magnitude of laparoscopic deformation significantly exceeds the magnitude of open deformation ($p = 0.0019$). This finding suggests that laparoscopic deformations have the potential to compromise surgical guidance to a potentially greater degree than the deformations associated with open surgery. Figure 4 shows three representative distributions of closest point distance error between preoperative, laparoscopic, and open organ shapes. Compared with the preoperative organ, laparoscopic deformation tends to produce more flattening of the right lobe than does open.

Our efforts to use the laparoscopic phantom setup described in Sec. 2.2 for validation are contingent on accurately replicating intraoperative deformation of the liver. Laparoscopic-to-open conversion was also simulated in the phantom for comparison of our applied deformation with clinically observed 95% confidence intervals. Open phantom deformation was imposed by removing all supporting ligaments and packing material beneath the left and right lobes to simulate typical intraoperative placement of laparotomy pads. We note that the confidence intervals of laparoscopic deformation are comparable to the porcine insufflation landmark error ranging between 5.8 and 11.5 mm reported by Johnsen et al.[17] and the open surgery surface error ranging between 5 and 20 mm reported by Clements et al.[41] As shown in Table 2, our phantom performs similarly to clinical behavior as demonstrated by magnitudes of laparoscopic and open deformation within the clinical confidence intervals. Our mock abdomen setup is designed to emulate a constant insufflation pressure that causes distension of the abdominal cavity and subsequent tension on the ligament attachments. Therefore, it is reasonable that the laparoscopic magnitude of deformation in our phantom is more consistent with 7-mm Hg than 14-mm Hg insufflation pressure. We do recognize that additional effects, such as the presence of ambient

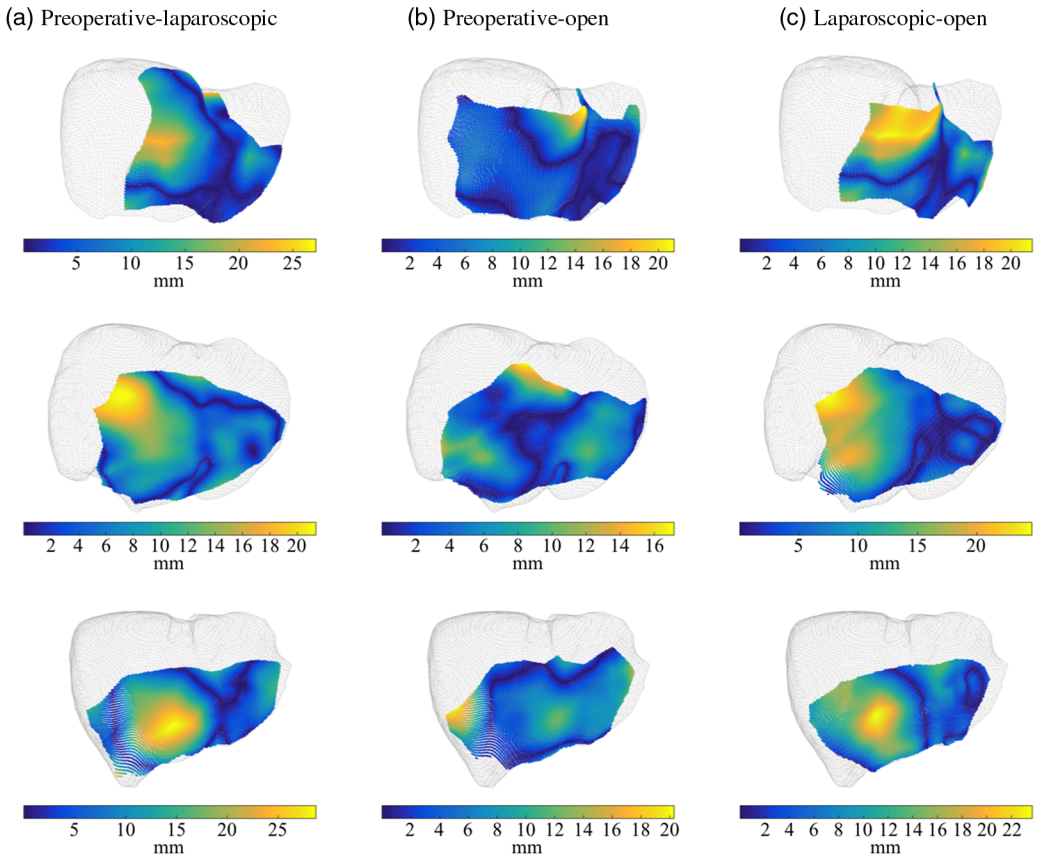

Fig. 4 Reconstructed closest point distance error from three representative cases among the $n = 25$ between (a) preoperative and laparoscopic surfaces, (b) preoperative and open surfaces, and (c) laparoscopic and open surfaces.

Table 2 Confidence intervals [LB, UB] in mm for preoperative-to-intraoperative MHD shape changes from the clinical series of laparoscopic-to-open conversion. MHD for respective changes in our phantom validation setup is also presented to provide a sense for the fidelity with which intraoperative deformation is reproduced.

	Clinical confidence interval	Phantom
Lap14mmHg	[7.7, 12.6]	
Lap7mmHg	[6.2, 11.9]	6.9
Open	[5.5, 9.3]	8.6

insufflation pressure on the organ, may contribute additional deformation beyond the capabilities of our phantom setup. However, this is expected to be of secondary importance because the total force applied to the exposed surface area of the liver is much smaller than the total force applied to the entire abdominal cavity, subsequently transmitted to the liver via ligament attachments.

3.2 *Evaluation of Deformation Correction*

We evaluate our nonrigid registration algorithm in a series of experiments that use the phantom and clinical data acquired in Secs. 2.1 and 2.2. These experiments include: (1) phantom comparison of the proposed nonrigid registration method with the method reported by Rucker et al., (2) comparison of local surface correction in clinical and phantom datasets, and (3) the effect of surface data extent on subsurface registration accuracy.

3.2.1 *Comparison of registration methods*

The three mobilization scenarios of the phantom were registered using intraoperative surface data collected through a port at the umbilicus by three methods: (a) the salient feature-weighted rigid registration by Clements et al.,[34] which is used to initialize both (b) the nonrigid registration method by Rucker et al.,[27] and (c) our proposed nonrigid control point registration for laparoscopic deformation of the liver. Average TRE over these cases was used to assess overall registration performance for the three methods. Since TRE samples from a spatially varying distribution of the underlying error, the proximity of targets to known data and the uniformity of their density can affect the observed TRE. Furthermore, TRE may also depend on the amount of applied deformation. We attempt to minimize target selection bias by considering a large number of target positions dispersed evenly throughout the volume of the phantom [Fig. 1(c)] and provide a reference for our reported TRE by characterizing the amount of deformation experienced by the phantom (Table 2).

TRE for the rigid and nonrigid registration methods is shown in Table 3 and qualitative registration results are shown in Fig. 5. Across the three mobilizations of the phantom, rigid registration on average produced TRE of 14.7 ± 1.2 mm. The nonrigid

Table 3 TRE (mean ± SD) in mm for simulated mobilization conditions of the phantom after rigid and nonrigid registration.

Phantom deformation	Rigid registration: Clements et al.	Nonrigid registration: Rucker et al.	Nonrigid registration: Control point supports
Left mobilization	13.2 ± 2.6	7.1 ± 3.5	5.9 ± 4.3
Right mobilization	16.2 ± 6.7	8.0 ± 5.5	7.0 ± 4.6
No mobilization	14.7 ± 6.5	8.5 ± 3.9	6.2 ± 4.1

correction method by Rucker et al. reduced average TRE to 7.9 ± 0.6 mm, representing a 46.3% improvement. On the other hand, the laparoscopic nonrigid registration method proposed in this work reduced TRE to 6.4 ± 0.5 mm, representing a 56.5% correction over rigid registration. Our proposed correction method performed 19.4% better on average ($p = 0.044$, two-sample t-test) than the method by Rucker et al. for deformations produced in the laparoscopic phantom setup. This improvement speaks toward the contributions of modeling the intraoperative load applied to ligaments, which are not accounted by Rucker et al., and reformulating the application of boundary conditions to make no incorrigible assumptions about the spatial profile of displacement on the support surfaces.

3.2.2 *Comparison of surface correction*

We explore clinical feasibility of our deformation correction approach through evaluating and comparing surface error in the phantom and in a retrospective analysis of the laparoscopic-to-open conversion series. Although surface error is a lacking metric due to uncertainty in surface correspondence and insensitivity to subsurface registration accuracy, appropriately measuring target error in clinical data is burdensome due to intraoperative imaging requirements. To reduce the impact of surface digitization noise and irregular spatial weighting of points, we use a reconstructed intraoperative surface from sparse data to ensure that the surface correction measure evenly weights error across the entire area of surface coverage.

Figure 6 shows the surface registration error for rigid registration in comparison with our laparoscopic deformation correction method. We consistently obtain low surface errors below 2 mm in all intraoperative organ configurations. Compared

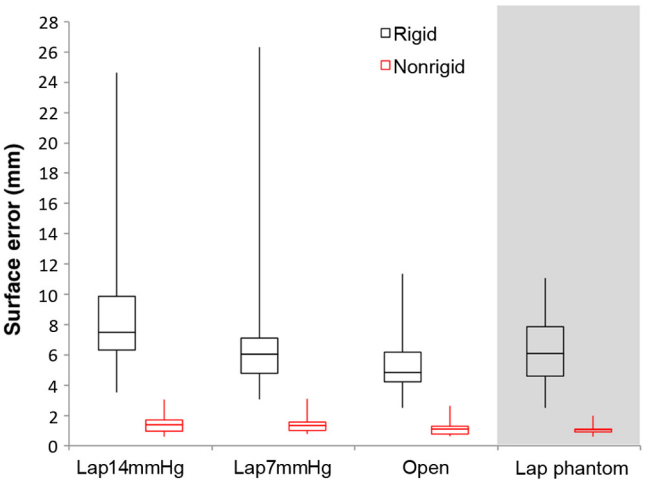

Fig. 6 Surface correction quartiles are shown for rigid and nonrigid registrations to each series of laparoscopic and open organ configurations. The gray panel displays the distribution of surface correction among all intraoperative phantom mobilizations and surface data extents.

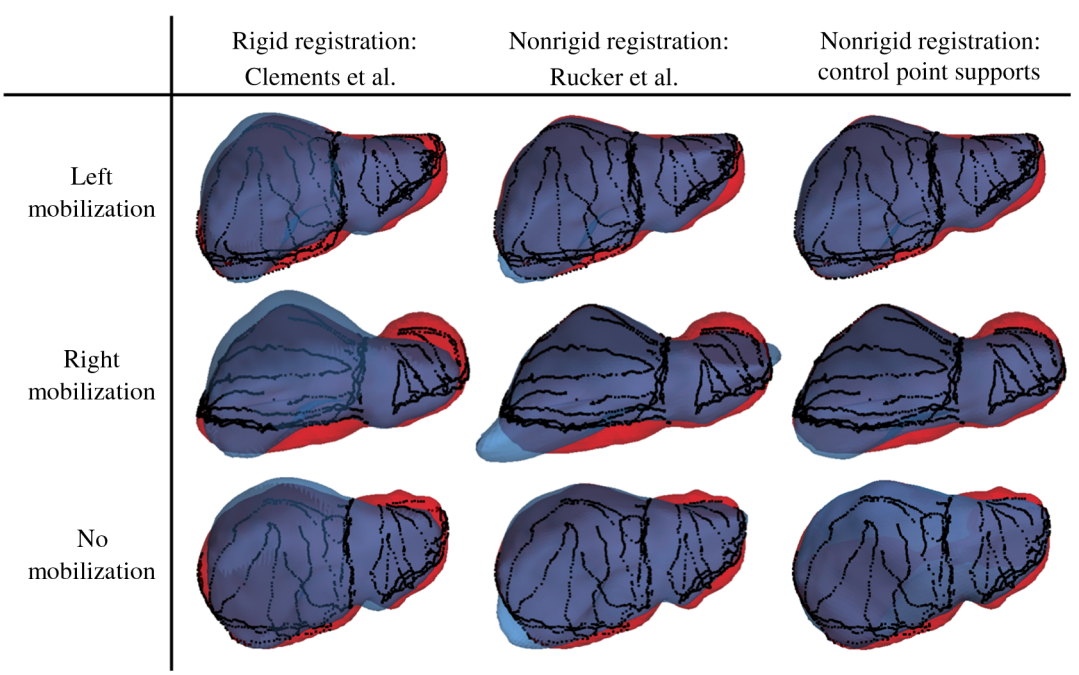

Fig. 5 Registered preoperative liver (blue) in comparison with the ground-truth intraoperative organ shape (red) for each organ deformation and registration technique. The sparse intraoperative data used to perform the registrations are overlaid in black. Attaining perfect alignment is challenging due to incomplete coverage of the intraoperative surface data.

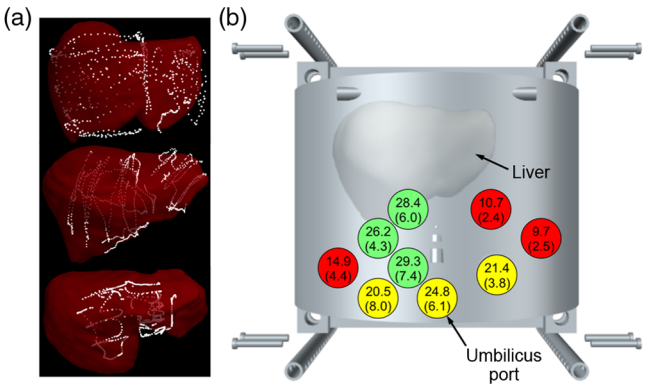

Fig. 7 (a) Variation in available surface data extents from clinical data: 31% (top), 20% (center), and 11% (bottom). (b) Average surface data extents through each of the nine ports of the phantom, standard deviation in parentheses. Lateral ports colored in red provide average extents of <15% of the organ surface. Periumbilical ports in yellow offer moderate extents between 20% and 25%, and ports placed in the medial right upper quadrant yield the best available surface extents, which exceed 25% on average.

with rigid, the nonrigid correction algorithm reduced surface error from 9.3 ± 5.4 mm to 1.4 ± 0.6 mm for standard insufflation pressure (Lap14mmHg), from 7.0 ± 4.6 mm to 1.4 ± 0.5 mm for reduced insufflation pressure (Lap7mmHg), and from 5.2 ± 2.0 mm to 1.1 ± 0.4 mm for open registration. Surface error for laparoscopic registrations of the phantom decreased from 5.5 ± 2.2 mm to 0.8 ± 0.4 mm after nonrigid correction. These reductions correspond to surface corrections of $84.8\% \pm 6.1\%$ for Lap14mmHg, $80.1\% \pm 7.0\%$ for Lap7mmHg, $78.7\% \pm 8.4\%$ for open organ configuration, and $85.4\% \pm 7.3\%$ for the phantom. While future subsurface validation work using intraoperative imaging is needed, these results show promise of our algorithm toward laparoscopic deformation correction in prospective clinical use.

3.2.3 *Impact of surface data extent*

As shown in Fig. 7(a), the amount of organ surface coverage from intraoperative sparse digitizations can be highly variable. For each intraoperative surface collection, we quantify the extent of organ surface coverage as the percentage of boundary nodes on the liver model contained within an alpha shape constructed around the sparse data. To identify potential sources of variable surface extent, we collected intraoperative surface data through the nine laparoscopic ports placed in the mock abdomen and computed their extents on the phantom as presented in Fig. 7(b). These results indicate that certain ports, especially those placed in the medial right upper quadrant, can produce better extent than more lateral or inferior ports. Across standard and lowered insufflation pressures, the average surface extent from clinical data was $21.96\% \pm 8.25\%$ ($N = 50$). In the phantom, two separate digitization strategies and three different organ mobilizations across nine ports produced an average extent of $20.65\% \pm 8.78\%$ ($N = 54$). Registration accuracy in the phantom as a function of extent is shown in Fig. 8. We observe that as surface extent increases, the capability of our proposed deformation correction algorithm improves. At extents >22%, the overall average TRE across all cases was

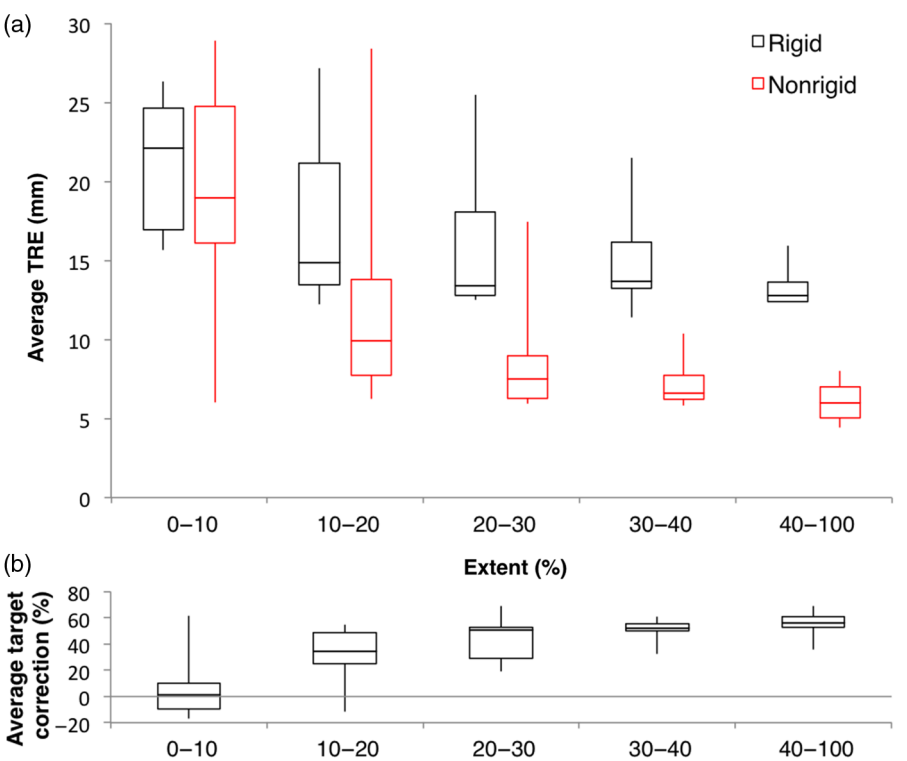

Fig. 8 Distributions of (a) TRE and (b) target correction with respect to the extent of intraoperative surface data. The box and whiskers represent the median, upper and lower quartiles, maximum, and minimum of TRE. Our nonrigid correction contributes little improvement over rigid registration at extents smaller than 10%. However, at extents >22%, the nonrigid correction algorithm offers a substantial improvement in TRE.

6.7 ± 1.3 mm, and all individual nonrigid registrations produced average TRE under 10 mm. Plantefève et al.[24] also observed similar behavior where nonrigid registration accuracy is superior at extents >20% of the total liver surface. We further show that the extents of typical clinical data acquisitions tend to lie on the cusp of this threshold. It is possible that more deliberate choices in port positioning for data collection may offer straightforward improvements to laparoscopic nonrigid registrations.

4 Discussion

Our registration method is distinct from other mechanics-based correction algorithms that apply boundary conditions derived directly from the positions of intraoperative surface points. Instead, the proposed approach leverages anatomical constraints in such a way that permits only deformations that can be produced by realistic intraoperative changes to the organ. This process is done by (1) identifying support surface regions associated with intraoperative changes to mechanical load, (2) constructing a set of model perturbations based on point load displacements on the support surfaces, (3) registering and reconstructing a configuration of point load displacements from the observed intraoperative surface, and (4) relaxing the model solution. Beyond the current application to laparoscopic liver deformation, this algorithm is generalizable to other deformable soft tissues. A key advantage to the approach is that steps (1) and (2) can be completed preoperatively. Therefore, the intraoperative computational burden only consists of determining an initial rigid registration between the model and intraoperative data, optimizing the control point perturbations, and performing the relaxation step. Without extensive code optimization, the entire intraoperative registration can be performed within 140 to 320 s on a single thread using a 4.0-GHz Intel Core i7 CPU for a liver model of 30,000 nodes and ~3000 intraoperative data points. However, significant acceleration of the optimization can be expected from parallelizing the closest point correspondence in the objective function or from reducing the tolerance.

In our experience, the choice of a linear model is not a principal source of error for deformation correction in the liver due to the existence of other practical limitations. Noise in data collection, irregular point density, and variable patterns of intraoperative surface digitizations introduce inconsistencies that affect registration outcomes. Scarcity of definitive hepatic features that could offer correspondence between intraoperative digitizations and the model surface is an additional barrier to achieving accurate registration. Furthermore, incomplete surface data extents that leave regions of the model unconstrained also limit overall registration accuracy. While we attempt to alleviate some of these challenges in this work through employing data resampling and salient feature weighting in the objective function of Eq. (18), these solutions do not fully resolve these issues and generally leave the problem ill-posed. However, the use of a linear model is unlikely to be ideal, and efficient nonlinear treatments[40,42] could be explored in future work to further improve registration accuracy. Another important aspect would be the incorporation of heterogeneities, such as the major vascular branches within the liver. It is likely that vessel-to-tissue interaction would alter the volumetric behavior of our model.

In our registrations, we find that the distance between an individual target and the closest surface data point used to perform the registration is moderately correlated with the individual TRE (Pearson's $r = 0.58$; 99% CI: 0.56 to 0.60). We expect that regions more distant from intraoperative surface data are prone to less accurate registration due to lack of model specificity. Ideally, errors of <5 mm across the volume of the liver would be desirable for guidance of hepatic resections. While surface error can be corrected past this threshold, comprehensive analysis of TRE across the full volume of the liver indicates that targets farther from anterior surface data tend to perform more poorly. With the magnitude of laparoscopic deformations exceeding those of open, it is likely more challenging to achieve TRE below 5 mm across the volume of the liver under laparoscopic operative conditions. Currently, the clinical data extent is sufficient to achieve corrections with <10 mm of error, which may be considered adequate though not ideal. It is reasonable to expect that increasing surface extent or incorporating subsurface data into the registration workflow could improve registration by increasing the reach of intraoperative data constraints. Future work will involve the development of methods to expand intraoperative data extent through improvements to noncontact methods of laparoscopic surface acquisition and the integration of tracked intraoperative ultrasound for the purpose of validating registration error *in vivo* and as a potential source of subsurface constraints for further improving laparoscopic deformation correction methods.

5 Conclusions

In this paper, we present an analysis of the extent of liver deformation among preoperative, laparoscopic, and open presentations as well as a technique for correcting deformation during image-guided laparoscopic liver surgery. Our analysis of deformation revealed that the most severe shape differences exist between preoperative and intraoperative presentations under routine insufflation conditions, which may compromise the planning stages of laparoscopic surgery. To compensate for this soft tissue deformation, we propose a correction algorithm that leverages anatomically load-bearing support surfaces of the liver to enforce model constraints and demonstrates superior deformation correction than previous realizations. Finally, we perform extensive studies to understand the influence of data coverage extent in both the phantom and clinical settings. We propose that image-guided laparoscopic liver surgery is achievable in practice with current techniques and careful consideration of the particular challenges introduced by the laparoscopic approach.

Disclosures

The authors of the paper declare no potential conflicts of interest.

Acknowledgments

This work has been supported by the National Institutes of Health (NIH) under Grant No. R01-CA162477 and the NIH-National Institute of Biomedical Imaging and Bioengineering training Grant No. T32-EB021937. We also would like to recognize the Vanderbilt University Medical Center Radiology Support Core for their assistance with imaging in our phantom study.

References

1. R. Ciria et al., "Comparative short-term benefits of laparoscopic liver resection: 9000 cases and climbing," *Ann. Surg.* **263**(4), 761–777 (2016).
2. A. A. Fretland et al., "Laparoscopic versus open resection for colorectal liver metastases: the OSLO-COMET randomized controlled trial," *Ann. Surg.* **267**(2), 199–207 (2018).

3. I. Dagher et al., "International experience for laparoscopic major liver resection," *J. Hepato-Biliary-Pancreatic Sci.* **21**, 732–736 (2014).
4. M. C. Halls et al., "Conversion for unfavorable intraoperative events results in significantly worst outcomes during laparoscopic liver resection: lessons learned from a multicenter review of 2861 cases," *Ann. Surg.* Pre-print, 1–7 (2017).
5. T. Lange et al., "Development of navigation systems for image-guided laparoscopic tumor resections in liver surgery," *Recent Results Cancer Res.* **167**, 13–36 (2006).
6. A. Ferrero et al., "Ultrasound-guided laparoscopic liver resections," *Surg. Endosc.* **29**, 1002–1005 (2015).
7. G. Wakabayashi et al., "Recommendations for laparoscopic liver resection: a report from the second international consensus conference held in Morioka," *Ann. Surg.* **261**(4), 619–629 (2015).
8. N. C. Buchs et al., "Augmented environments for the targeting of hepatic lesions during image-guided robotic liver surgery," *J. Surg. Res.* **184**(2), 825–831 (2013).
9. T. P. Kingham et al., "Evolution of image-guided liver surgery: transition from open to laparoscopic procedures," *J. Gastrointest. Surg.* **17**, 1274–1282 (2013).
10. C. W. Hammill et al., "Evaluation of a minimally invasive image-guided surgery system for hepatic ablation procedures," *Surg. Innov.* **21**(4), 419–426 (2014).
11. S. Thompson et al., "Accuracy validation of an image guided laparoscopy system for liver resection," *Proc. SPIE* **9415**, 941509 (2015).
12. Y. Song et al., "Locally rigid, vessel-based registration for laparoscopic liver surgery," *Int. J. Comput. Assisted Radiol. Surg.* **10**, 1951–1961 (2015).
13. M. Fusaglia et al., "A clinically applicable laser-based image-guided system for laparoscopic liver procedures," *Int. J. Comput. Assisted Radiol. Surg.* **11**, 1499–1513 (2016).
14. C. Song et al., "Mechanical properties of the human abdominal wall measured in vivo during insufflation for laparoscopic surgery," *Surg. Endosc.* **20**(6), 987–990 (2006).
15. M. L. N. G. Malbrain, Y. Peeters, and R. Wise, "The neglected role of abdominal compliance in organ-organ interactions," *Crit. Care* **20**, 67 (2016).
16. S. Vijayan et al., "Liver deformation in an animal model due to pneumoperitoneum assessed by a vessel-based deformable registration," *Minimally Invasive Ther. Allied Technol.* **23**, 279–286 (2014).
17. S. F. Johnsen et al., "Database-based estimation of liver deformation under pneumoperitoneum for surgical image-guidance," *Lect. Notes Comput. Sci.* **9350**, 450–458 (2015).
18. Y. Masutani and F. Kimura, "A new modal representation of liver deformation for non-rigid registration in image-guided surgery," *Int. Congr. Ser.* **1230**, 20–26 (2001).
19. D. M. Cash et al., "Compensating for intraoperative soft-tissue deformations using incomplete surface data and finite elements," *IEEE Trans. Med. Imaging* **24**(11), 1479–1491 (2005).
20. P. Dumpuri et al., "Model-updated image-guided liver surgery: preliminary results using surface characterization," *Prog. Biophys. Mol. Biol.* **103**(2–3), 197–207 (2010).
21. M. Allan et al., "Non rigid registration of 3D images to laparoscopic video for image guided surgery," *Lect. Notes Comput. Sci.* **9515**, 109–116 (2015).
22. A. Myronenko and X. Song, "Point set registration: coherent point drift," *IEEE Trans. Pattern Anal. Mach. Intell.* **32**(12), 2262–2275 (2010).
23. S. Suwelack et al., "Physics-based shape matching for intraoperative image guidance," *Med. Phys.* **41**, 111901 (2014).
24. R. Plantefève et al., "Patient-specific biomechanical modeling for guidance during minimally-invasive hepatic surgery," *Ann. Biomed. Eng.* **44**(1), 139–153 (2016).
25. D. Reichard et al., "Projective biomechanical depth matching for soft tissue registration in laparoscopic surgery," *Int. J. Comput. Assisted Radiol. Surg.* **12**(7), 1101–1110 (2017).
26. L. Maier-Hein et al., "Comparative validation of single-shot optical techniques for laparoscopic 3-D surface reconstruction," *IEEE Trans. Med. Imaging* **33**(10), 1913–1930 (2014).
27. D. Rucker et al., "A mechanics-based nonrigid registration method for liver surgery using sparse intraoperative data," *IEEE Trans. Med. Imaging* **33**(1), 147–158 (2014).
28. L. W. Clements et al., "Evaluation of model-based deformation correction in image-guided liver surgery via tracked intraoperative ultrasound," *Med. Imaging* **3**(1), 1–10 (2016).
29. J. M. Sullivan et al., "A three-dimensional mesh generator for arbitrary multiple material domains," *Finite Elem. Anal. Des.* **25**, 219–241 (1997).
30. D. M. Cash et al., "Concepts and preliminary data toward the realization of image-guided liver surgery," *J. Gastrointest. Surg.* **11**(7), 844–859 (2007).
31. J. S. Heiselman et al., "Emulation of the laparoscopic environment for image-guided liver surgery via an abdominal phantom system with anatomical ligamenture," *Proc. SPIE* **10135**, 101352W (2017).
32. R. A. Lathrop et al., "Minimally invasive holographic surface scanning for soft-tissue image registration," *IEEE Trans. Biomed. Eng.* **57**(6), 1497–1506 (2010).
33. A. L. Simpson et al., "Comparison study of intraoperative surface acquisition methods for surgical navigation," *IEEE Trans. Biomed. Eng.* **60**(4), 1090–1099 (2013).
34. L. W. Clements et al., "Robust surface registration using salient anatomical features for image-guided liver surgery: algorithm and validation," *Med. Phys.* **35**(6), 2528–2540 (2008).
35. J. A. Collins et al., "Improving registration robustness for image-guided liver surgery in a novel human-to-phantom data framework," *IEEE Trans. Med. Imaging* **36**(7), 1502–1510 (2017).
36. M.-P. Dubuisson and A. K. Jain, "A modified Hausdorff distance for object matching," in *Proc. Int. Conf. on Pattern Recognition*, pp. 566–568 (1994).
37. H. S. Kim et al., "Bidirectional local distance measure for comparing segmentations," *Med. Phys.* **39**(11), 6779–6790 (2012).
38. C. O. Horgan and L. E. Payne, "Saint-Venant's principle in linear isotropic elasticity for incompressible or nearly incompressible materials," *J. Elast.* **46**, 43–52 (1997).
39. F. Devernay, "CMinpack," 1.3.4, https://github.com/devernay/cminpack (2014).
40. J. Georgii and R. Westermann, "Corotated finite elements made fast and stable," in *Proc. of the 5th Workshop on Virtual Reality Interaction and Physical Simulation (VRIPHYS)*, pp. 11–19 (2008).
41. L. W. Clements et al., "Organ surface deformation measurement and analysis in open hepatic surgery: method and preliminary results from 12 clinical cases," *IEEE Trans. Biomed. Eng.* **58**(8), 2280–2289 (2011).
42. S. Marschesseau, S. Chatelin, and H. Delingette, "Non linear biomechanical model of the liver: hyperelastic constitutive laws for finite element modeling," in *Biomechanics of Living Organs*, Y. Payan and J. Ohayon, Eds., pp. 602–623, Elsevier/Academic Press, London (2017).

Biographies for authors are not available.